scientific reports

Check for updates

OPEN

A dual path graph neural network framework for dementia diagnosis

Denghui Zhang[1] & Chenxuan Zhu[2]✉

Dementia typically results from damage to neural pathways and the consequent degeneration of neuronal connections. Graph neural networks (GNNs) have been widely employed to model complex brain networks. However, leveraging the complementary temporal, spatial, and spectral features for diagnosing neurocognitive disorders remains challenging. To address this issue, we propose a Bi-path Multi-scale Graph Neural Network (Bi-MCGNN), which integrates two paths : one focusing on time and spatial relationships, and the other on spatial and frequency patterns. By unifying these pathways, Bi-MCGNN integrates diverse brain features into a single framework. In order to more effectively represent brain networks, we designed specialized correlation matrixs to reinforce the constructed graph. We then performed multi-scale graph convolution to analyze brain connectivity at varying resolutions-from fine-grained to more extensive patterns, and ultimately employed an attention mechanism to enhance features across different domains. Extensive experiments on two real-world datasets demonstrate that our model outperforms state-of-the-art baselines.

Keywords Electroencephalography, Dementia, Graph neural network, Neurocognitive disorders, Correlation matrix

With the accelerating aging of the global population, dementia has emerged as a significant challenge impacting public health and socioeconomic systems. Its high prevalence and complex pathological mechanisms place substantial demands on healthcare resources and caregiving infrastructures. Currently, no cure exists for dementia. however, early detection and intervention can significantly slow their progression. Consequently, there is an urgent need to develop low-cost, reliable, and easily implementable detection methods[1]. In the realm of computer-aided detection for neurocognitive disorders, research has primarily focused on Magnetic Resonance Imaging (MRI)[2] and Positron Emission Tomography (PET). Although these modalities offer high detection accuracy, they are expensive and often inaccessible, with diagnoses typically occurring only after significant neurodegenerative changes have manifested. In contrast, electroencephalography (EEG) presents a low-cost, noninvasive,and user-friendly alternative. EEG utilizes scalp (or intracranial) electrodes to measure postsynaptic potentials generated by brain neurons, revealing complex interconnections between adjacent and distant cortical regions[3]. Brain connectivity analysis is believed to provide deeper insight into various neurodegenerative diseases, helping unraveling their underlying mechanisms[4,5].

By representing EEG data in graph form, researchers can explore functional connections and interactions between different regions of the brain, offering valuable information about brain function and its disorders[6]. Graph-based studies have demonstrated that AD patients exhibit abnormalities in cross-frequency coupling (CFC) between different frequency bands in functional connectivity[7,8], a reduction in network complexity[9], and a loss of small-world organization[10]. These characteristics can be evaluated using graph metrics such as clustering coefficients and path lengths. Recently, the application of Graph Neural Networks to EEG data classification has grown significantly, attracting widespread attention in the research community[11–13]. Unlike traditional methods such as multi-layer perceptrons (MLPs) or convolutional neural networks, GNNs treat each EEG channel as a node in a graph, learning the interactions between them in a flexible manner. This approach is particularly well-suited for extracting complex spatial structural features from EEG data[14,15]. However, applying graph-based EEG techniques to neurocognitive disorder diagnosis still presents several challenges.

C1: How to utilize the complementarity between the spatial-spectral-temporal domain information efficiently. Information from the temporal and spectral domain in the spatial domain of EEG signals typically exhibits varying levels of activation. For example, Fig.1 illustrates the differences between the temporal and spectral domains in the spatial domain of EEG signals with varying degrees of neurocognitive impairment. In the spatiotemporal domain, patients with more severe neurocognitive impairment exhibit greater temporal activation fluctuations or irregularities, whereas healthy controls typically maintain similar activation patterns across different time periods. Spectral analysis shows that, compared with healthy controls, cognitively impaired

[1]College of Information Science and Technology, Zhejiang Shuren University, Hangzhou 310015, China. [2]School of Information Engineering, Huzhou University, Huzhou 313000, China. ✉email: HanHenry99@163.com

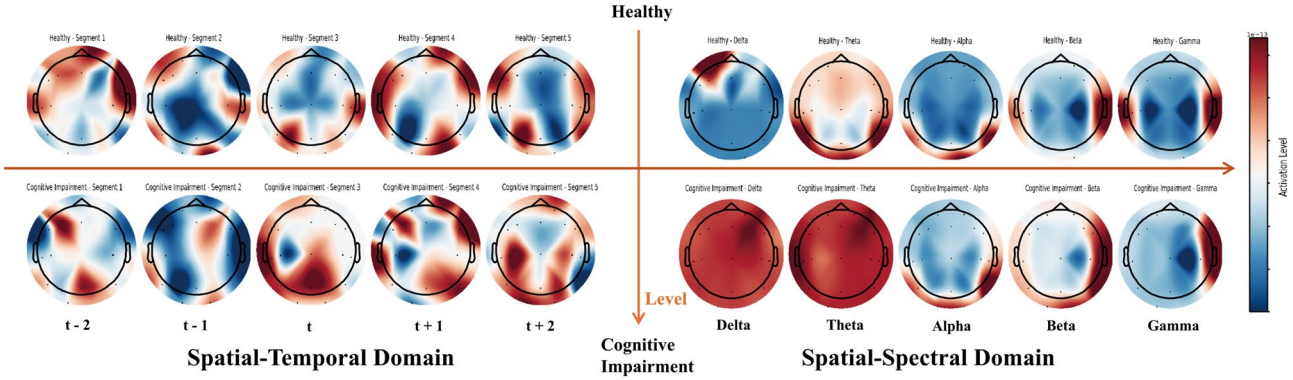


Fig. 1. The complementarity among spatial-spectral-temporal domain features. Topographic maps of the brain indicate that the activation levels of temporal and spectral information in the spatial domain vary across different degrees of cognitive impairment.

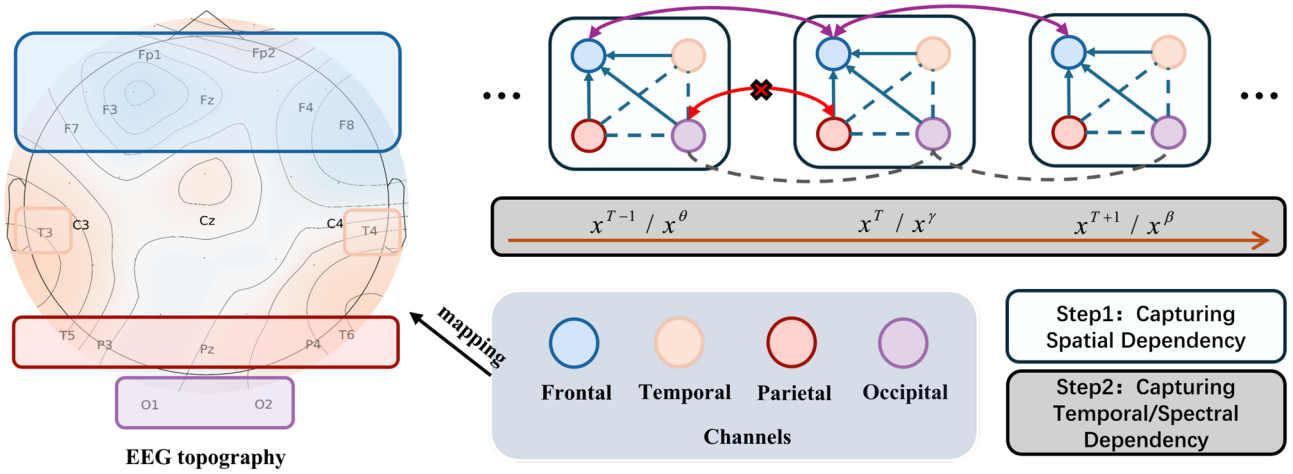


Fig. 2. The graph construction captures dependencies by creating individual graphs for each time window or frequency band of EEG signals. In Step 1, the graph neural network (GNN) extracts spatial dependencies within each graph (e.g., frontal channels in individual graphs). In Step 2, the domain encoder captures dependencies between corresponding brain regions (channels) across different time windows or frequency bands, such as the sequence $[x^{T-1}, x^{T}, x^{T+1}]$. However, this approach neglects cross-temporal correlations between heterogeneous sensors (e.g., the occipital region in x^{T-1} and the parietal region in x^{T}), thereby failing to model comprehensive spatio-temporal ST dependencies.

patients demonstrate higher activation in low-frequency bands such as Delta and Theta. By contrast, healthy controls usually have higher activation in the high-frequency bands (Beta, Gammy), indicating that high-frequency activity is closely associated with brain cognitive function. Numerous studies employ deep learning methods to extract spatiotemporal (ST) or spatial-spectral (SS) information for diagnosing disease progression. These approaches can be categorized into two main types: one focusing on the spatio-temporal domain[16,17] and the other on the spatial-spectral domain[18,19]. Although both approaches have achieved satisfactory performance, they overlook the complementarity between temporal, spatial, and spectral information. Consequently, effectively extracting temporal-spatial-spectral information remains a challenging task (Fig. 2).

C2: How to capture the correlations between different EEG electrode channels under varying timestamps (DCDT) and across different spectral domains (DCDB) in Dementia EEG data . In patients with neurocognitive disorders, the neural connections and synchronization of electrical activity between different brain regions are often disrupted, leading to a significant decrease in the temporal variability of EEG signals. In the frequency domain, cross-frequency coupling between EEG bands exhibits significant differences across various stages of the disease. To capture spatio-temporal (ST) and spatial-spectral (SS) dependencies, a common approach is to partition EEG recordings into time windows or frequency bands and construct separate graphs for each window or band. Subsequently, Graph Neural Networks (GNNs) are used to model dependencies between electrode channels across different time windows or frequency bands, incorporating domain-specific encoders (e.g., spectral or temporal encoders) to further model complex associations. However, this method processes each

graph independently[16,18], overlooking correlations between electrodes (brain regions) across time windows or frequency bands, as shown in Figure 2.

Current EEG-based dementia diagnostic approaches exhibit several fundamental limitations. First, although frequency-band partitioning (e.g., dividing delta/theta for PLI and alpha/beta/gamma for AEC-c in Wu[20] et al, or deploying SVD and entropy-based features in Klepl et al[21]) can extract multi-band information, these methods frequently overlook cross-frequency couplings that are integral to neurodegenerative biomarkers. Similarly, GNN-based methods such as klepl et al. [(which use PSD-similarity graphs), wu et al.(which use permutation-test-derived topologies), and Klepl et al.[19] (which use static functional connectivity graphs) show promise in modeling spatial dependencies but tend to oversimplify temporal dynamics or neglect frequency-band interactions. For instance, Cao et al.'s DSL-GNN[18] focuses solely on directional spatial connectivity, without capturing how delayed neural responses modulate correlations. Second, multi-domain frameworks-such as ST-GCN[16], CNN-ViT hybrids[22], and Sanati et al.[23] often rely on hardcoded functional connectivity or isolated feature streams, thereby constraining their ability to adapt to patient-specific spatial-spectral coupling patterns and forfeiting important inter-domain synergies. Finally, current graph construction methods (e.g., Radwan et al.[17], which employs Granger causality, or simple concatenation-based fusions) suffer from physiologically implausible assumptions by overlooking neuroanatomical priors (e.g., time-delay decay [DCDT] and cross-frequency coupling [DCDB]). These limitations underscore the need for more adaptive and physiologically grounded approaches that can capture the full complexity of dementia-related EEG dynamics.

To address the aforementioned limitation, we propose a novel method called the Bi-path multi-scale graph neural network (Bi-MCGNN), which comprises three key components: the Bi-path architecture, FC graph construction, and FC graph convolution. These components work together to capture comprehensive spatio-temporal (ST) and spatial-spectral (SS) dependencies within dementia EEG data. For graph construction, we introduce an FC graph to establish full connections between all electrode channels across all timestamps and frequency bands, enabling the model to fully capture dependencies within the EEG data while considering correlations between DCDT and DCDB. To enhance the FC graph, we incorporate the physiological significance of dementia EEG data from both spatio-temporal and spatial-spectral perspectives. In the spatio-temporal domain, we introduce a decay matrix that accounts for the temporal distances between timestamps, assigning higher correlations to those that are temporally closer. This propose ensures that channels with proximal temporal locations exhibit stronger correlations than those with more distant temporal locations. In the spatial-spectral domain, we develop a coupling matrix that considers cross-frequency interactions, assigning higher correlations to frequency band combinations with stronger coupling. This approach ensures that combinations with higher coupling demonstrate stronger correlations compared to those with lower coupling.

We then propose the Bi-path architecture to effectively capture dependencies in dementia EEG data within the FC graph. While simple methods may extract only spatio-temporal (ST) or spatial-spectral (SS) information for dementia diagnosis, we recognize that such approaches may overlook the complementary nature of information across spatial, spectral, and temporal domains. Additionally, simple feature concatenation fails to explicitly capture the potential relationships between different features. To address these issues, we propose a bi-path FC graph convolution architecture that employs moving windows of a specific size to slide along the graph. Within each window, graph convolution is applied to update node features through edge propagation. After processing with parallel bi-path GNNs, the updated features are input into Bi-Path Attention Fusion (BAF), which dynamically adjusts the contribution of features, suppressing irrelevant or noisy ones to obtain the final representation.

In summary, our contributions are threefold. First, we propose a novel graph-based dual-path structure, comprising spatial-temporal and spatial-spectral paths, which integrates spatio-temporal-spectral features within a unified framework. Additionally, we introduce an adaptive feature fusion method that allocates feature weights and explicitly captures complex inter-feature relationships. Second, we propose decay and coupling matrices to enhance the constructed fully-connected (FC) graph by incorporating the internal correlations of DCDT and DCDB, facilitating more comprehensive dependency modeling. Furthermore, we propose a multi-scale graph convolution that captures both local and global information through multi-scale receptive fields and introduces learnable fusion weights, enabling the model to dynamically adjust the contributions of features at various scales, thus enhancing its expressive capability. Third, extensive experiments on two benchmark datasets demonstrate the method's strong performance, with results indicating a notable improvement in detection accuracy.

Related work

In recent years, the use of electroencephalography (EEG) for diagnosing neurocognitive disorders has gained significant attention, primarily due to EEG's capacity to effectively capture the functional states of various regions in the cerebral cortex. Additionally, its high temporal resolution and sequential nature enable real-time monitoring of rapid neural activity changes and dynamic patterns within time-series data.

Early studies primarily focused on extracting temporal, frequency-domain, and spatial features through various methods for disease classification. Temporal analysis, for instance, captures fluctuations in neural activity by calculating statistical measures such as mean, variance, and standard deviation[24]. Frequency-domain analysis, typically employing Fourier transforms, extracts spectral features (e.g., delta,theta and beta waves) to identify abnormal brain activity patterns[25–28]. Spatial analysis, on the other hand, uses spatial filtering techniques to extract features such as independent components and functional connectivity, thereby capturing the cooperative relationships between different brain regions[29].

However, these methods often rely heavily on prior knowledge. The advent of deep learning techniques aims to address the limitations of traditional machine learning approaches. Ieracitano et al.[30] analyzed 19-channel EEG recordings by evaluating the power spectral density (PSD) and representing the corresponding spectral

curves as two-dimensional grayscale images (PSD images). They developed a customized convolutional neural network (CNN) to automatically extract relevant frequency features from these images. Similarly, Rad et al.[31] converted EEG signals into two-dimensional grayscale images, achieving accurate Alzheimer's disease classification by learning complex time-frequency features and lesion information. In recent years, semi-supervised learning (e.g., pseudo-label propagation based on graph convolutions)[32,33] and self-supervised learning (e.g., temporal contrastive predictive coding[34]) have achieved remarkable advances in various domains such as image/video analysis. In the context of EEG analysis, semi-supervised (pseudo-label co-training) and self-supervised (temporal context prediction) approaches leverage the associative attributes of unlabeled EEG data, effectively addressing the scarcity of EEG annotations and the issue of inter-subject distribution drift. Jiang et al.[35] employed unsupervised pretraining to obtain a generalized perceptual capacity for EEG signals. Fouladi et al.[36] proposed enhanced convolutional neural network (CNN) and convolutional autoencoder (conve-ae) models to more efficiently extract time-frequency features from EEG signals of Alzheimer's disease patients.

The complexity of EEG necessitates models capable of capturing interactions between electrode channels, which reflect coordinated activities across various brain regions. In recent years, the use of Graph Neural Networks (GNNs) in EEG data classification has grown substantially, as GNNs are well-suited to address the unique challenges of EEG analysis, particularly in extracting spatial structural features. Klepl et al.[19] estimated functional connectivity brain graphs from EEG signals and trained GNN models to leverage the spatial structure of EEG data for feature extraction, pattern discovery, and predictions based on the complex interactions between electrodes. Cao et al.[18] introduced a novel Directed Structure Learning Graph Convolutional Neural Network (DSL-GNN) to analyze imaging graphs of Effective Brain Connectivity (EBC) and PSD features, extracting spatial-domain spectral features from EEG. Radwan et al.[17] classified EEG signals using GNN models and further explored the use of Granger causality as a measure of directed connectivity.

Multi-domain feature extraction can comprehensively capture EEG activity patterns in patients with neurocognitive disorders, overcoming the limitations of single-domain analyses[37,38]. This approach provides more thorough and detailed diagnostic insights. For instance, Shan et al.[16] proposed a dynamic spatiotemporal graph convolutional network (ST-GCN) that fully exploits the constrained spatial topology of functional connectivity and the discriminative dynamic temporal information encoded by one-dimensional convolutions to capture the spatiotemporal features of dementia-related EEG. Chen et al.[22] combined CNN and Vision Transformer (ViT)[39] components to separately capture temporal-spectral features.

While existing Alzheimer's disease (AD) diagnostic methods have achieved high accuracy, they often neglect the integration of multi-domain features. To address these gaps, we propose BI-MCGNN, a model that simultaneously captures the complementarity, heterogeneity, and signal correlations among spatial, spectral, and temporal features.

Methodology

Problem formulation

Given a dataset D consisting of n labelled EEG samples $\{X_j, y_j\}_{j=1}^{n}$, each sample $X_j \in \mathbb{R}^{N\times L}$ is collected N Electrode channels with T timestamps and B bands. Our objective is to learn an effective mapping function between graph and Cognitive states. Given spatial-temporal graph $G^T$and spatial-spectral graph G^B, the Cognition recognition problem can be defined as $Y = F\left(G^T, G^B\right)$, where Y denotes the recognition classification and F denotes the mapping function. For more information on the training pipeline, please refer to supplementary material A.1.

Bi-FC graph construction

Spatial-temporal graph construction

Given an EEG sample$X \in \mathbb{R}^{N\times L}$, we devide the signals from each channels into multiple patches by considering the local temporal patterns within EEG data . With a patch size of p, we obtain $\{X_t\}_{t=1}^{L'}$ from X, where t is the patch index representing a timestamp, and each $X_t \in \mathbb{R}^{N\times p}$. L' denotes the number of segmented patches, calculated as $L' = \left[\frac{L}{p}\right]$, where [.] represents the segmention operation. Each X_t contains segmented signals from N channels, i.e., $X_t = \{x_{t,i}\}_{i=1}^{N}$, where $x_{t,i} \in \mathbb{R}^p$

Afterward, we utilize an encoder f_c to handle the segmented signals within each window. Importantly, this encoder functions at the channel level to extract channel-level features, represented as $x'_{t,i} = f_c(x_{t,i})$. In addition, to preserve the directionality among patches, i.e., the relative positional information of patches. we implement positional encoding inspired by attention[40]. In detail, for the i-th channel, positional encoding, as illustrated in Eq. (1), is integrated into the channel features, such that $z_{t,i} = f_{pe}(t) + x'_{t,i}$, indicating the channel features that have been enhanced through positional encoding. Here, c denotes the c-th feature within the channel features, p represents different timestamps.

$$\vec{p}_p^{(c)} = f_{pe}(p)^{(c)} := \begin{cases} \sin(\omega_k \cdot p) & \text{if } c = 2k, \\ \cos(\omega_k \cdot p) & \text{if } c = 2k+1 \end{cases} \tag{1}$$

With the learned channel features across multiple patches, we can then proceed to construct an FC graph that interconnects all channels across these patches by additionally considering the correlations between DCDT .

In this context, we quantify the similarity between two EEG channels by employing a simple yet effective measure, the dot product, as shown in Eq.(2), where $t, r \in [1, L']$ index temporal segments (EEG patches) and $i, j \in [1, N]$ denote electrode channels indices. Here, we optimize EEG feature representation and similarity

computation by learning independent projection matrices for different channels and introducing a scaling factor , where W_i and W_j are the learnable weights, $\sqrt{d}$ is the dimension-aware scaling factor. Further, the softmax function restricts the correlations within [0,1].

$$e_{tr,ij} = \frac{(z_{t,i}w_i) \cdot (z_{r,j}w_j)^T}{\sqrt{d}} \tag{2}$$

Finally, we derive the FC graph $G^T = (Z^T, E^T)$, where $Z^T = \{\{z_{t,i}\}_{i=1}^{N}\}_{t=1}^{L'}$, and $E = \{\{e_{tr,ij}\}_{i,j=1}^{N}\}_{t,r=1}^{L'}$. E is denoted as the adjacent matrix of the FC graph, whose elements represent the correlations between channels among all patches. The graph G^B encompasses not only temporal correlations between timestamps and spatial correlations in each timestamp, but also additionally includes the correlations between DCDT, enabling us to model the comprehensive ST dependencies within Dementia EEG data.

Input: $\mathbf{X} \in \mathbb{R}^{N \times L}$: Raw EEG signals (N channels, L samples)
B: Number of frequency bands (e.g., $\{\delta, \theta, \alpha, \beta, \gamma\}$)
extract_PSD$(\cdot)$: PSD extraction function
$f_{\text{pe}}(\cdot)$: Positional encoding (Eq.1)
sim$(\cdot,\cdot)$: Similarity metric (Eq.3)
Output: $\mathcal{G}_B = (\mathbf{Z}_B, \mathbf{E}_B)$: Functional connectivity graph
$\mathbf{Z}_B = \{\mathbf{z}_{b,i} \mid i = 1, \ldots, N\}_{b=1}^{B}$: Node features
$\mathbf{E}_B = \{e_{bq,ij} \mid i, j = 1, \ldots, N\}_{b,q=1}^{B}$: Edge weights

Step 1: Multi-band PSD Feature Extraction
for $b \leftarrow 1$ **to** B **do**
  $\mathbf{X}_b \leftarrow$ BandpassFilter$(\mathbf{X}, f_b)$ // Extract band b signals
  for $i \leftarrow 1$ **to** N **do**
    $\mathbf{x}'_{b,i} \leftarrow$ extract_PSD$(\mathbf{x}_{b,i})$ // Compute PSD features
  end
end

Step 2: Positional Encoding
for $b \leftarrow 1$ **to** B **do**
  for $i \leftarrow 1$ **to** N **do**
    $\mathbf{z}_{b,i} \leftarrow f_{\text{pe}}(b) + \mathbf{x}'_{b,i}$ // Feature enhancement
  end
end

Step 3: Cross-band Connectivity Construction
Initialize $\mathbf{E}_B \leftarrow \emptyset$
for $b \leftarrow 1$ **to** B **do**
  for $q \leftarrow 1$ **to** B **do**
    for $i \leftarrow 1$ **to** N **do**
      for $j \leftarrow 1$ **to** N **do**
        $e_{bq,ij} \leftarrow \text{sim}(\mathbf{z}_{b,i}, \mathbf{z}_{q,j})$ // DCDB metrics
        $\mathbf{E}_B \leftarrow \mathbf{E}_B \cup \{e_{bq,ij}\}$
      end
    end
  end
end

Step 4: Graph Assembly
$\mathbf{Z}_B \leftarrow \{\{\mathbf{z}_{b,i}\}_{i=1}^{N}\}_{b=1}^{B}$
return $\mathcal{G}_B \leftarrow (\mathbf{Z}_B, \mathbf{E}_B)$

Algorithm 1. Spatial-spectral graph construction from multi-band EEG.

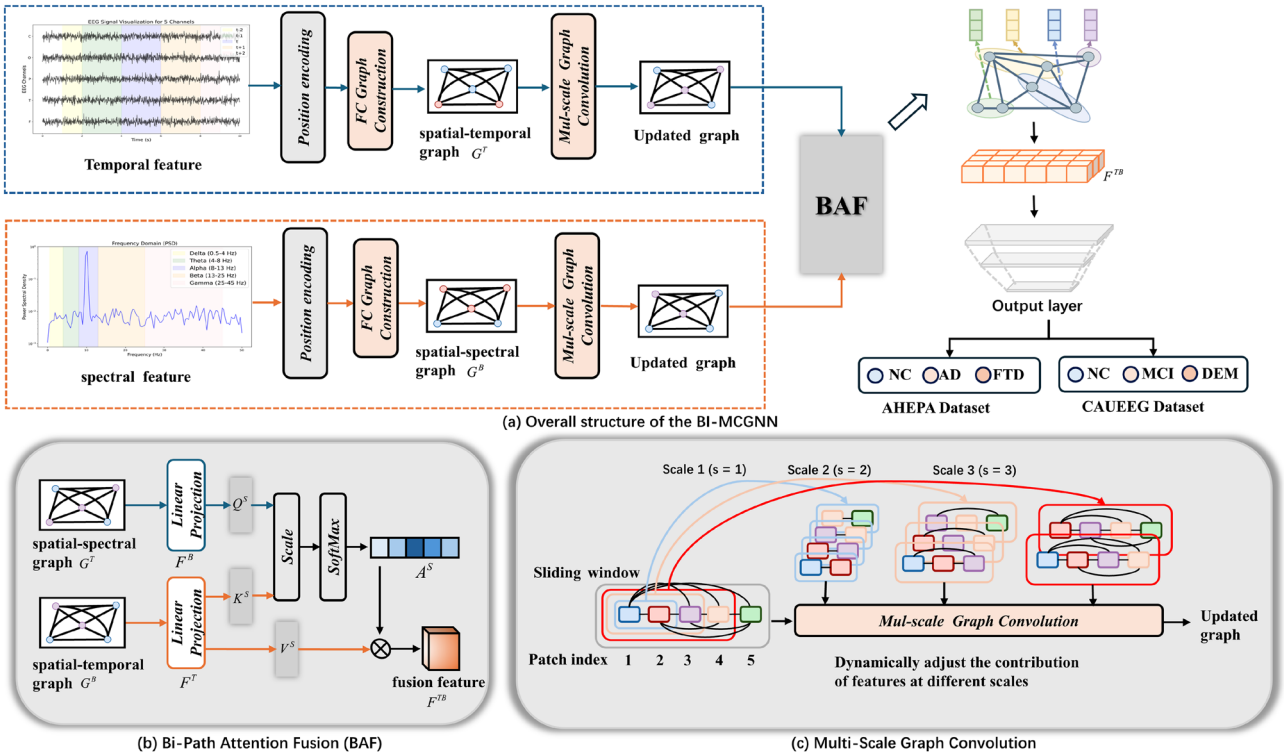


Fig. 3. Overall Structure of the BI-MCGNN. (**a**) The EEG samples are first divided into multiple patches, with signals from each channel processed to learn channel-level features through domain encoders within each patch. Positional encoding is then applied to the features from different patches, followed by fully connected (FC) graph construction and convolution, which leads to the Bi-Path Attention Fusion (BAF) of the two paths. This process ultimately generates the classification results. (**b**) Bi-Path Attention Fusion (BAF): BAF dynamically adjusts the contributions of graph features, suppressing irrelevant or noisy features to obtain the final representation. (**c**) Multi-Scale Graph Convolution: Moving windows of different scales slide along the graph. Within each scale, multi-scale graph convolution is performed to update node features through edge propagation, capturing both local and global information.

Spatial-spectral graph construction

By considering the distinct spectral domain patterns in each EEG sample $X \in \mathbb{R}^{N\times L}$, we extract PSD features from the relevant frequency bands, as illustrated in Fig.3. These features extracted from different channels and the correlation among channels are converted to spatial-spectral graphs. we create $\{X_b\}_{b=1}^{B}$ from X, where b is the band index representing a band, and $X^B = (x_\sigma, x_\theta, x_\alpha, x_\beta, x_\gamma)$. B denotes the number of extracted bands. Each X_b contains signals from N channels. Similarly, we employ an encoder to process the signals within each spectral domain. Specifically, for the i-th channels , positional encoding, as shown in Eq.(1), is introduced into channels features, e.g., $z_{b,i} = f_{pe}(b) + x'_{b,i}$ representing the channels features enhanced by positional encoding. Here, p represents different bands. With the extracted PSD features across multiple bands, we can then proceed to construct an FC graph that interconnects all PSD across these bands by additionally considering the correlations between DCDB.

$$e_{tr,ij} = \frac{(z_{b,i}w_i)\cdot(z_{q,j}w_j)^T}{\sqrt{d}} \tag{3}$$

We further quantify the similarity between two channels across different bands using a method similar to the aforementioned approach, as shown in Eq. (3). Finally, we derive the FC graph $G^B = (Z^B, E^B)$, where $Z^B = \{\{z_{b,i}\}_{i=1}^{N}\}_{b=1}^{B}$, and $E = \{\{e_{bq,ij}\}_{i,j=1}^{N}\}_{b,q=1}^{B}$. E is denoted as the adjacent matrix of the FC graph, whose elements represent the correlations between channels among all bands. The graph G^B encompasses not only spectral correlations and spatial correlations in each domain, but also additionally includes the correlations between DCDT, enabling us to model the comprehensive SS dependencies within Dementia EEG data, the complete spatial-spectral Graph onstruction is provided in Algorithm 1.

Correlation matrix

The FC graphs G^T and G^B are constructed solely based on the similarity of EEG channels across patches and frequency bands, without accounting for the correlations between channels within the same patch or band.

However, from a temporal perspective, channels that are farther apart in time are expected to exhibit weaker correlations than those that are temporally proximate. Similarly, the energy variations across different frequency bands may not be independent but interrelated, reflecting overall changes in brain functional connectivity. Motivated by these insights, we designed two association matrices: a temporal decay matrix, which attenuates correlations based on temporal distance, and a spectral coupling matrix, which accounts for the strength of coupling between frequency bands. These matrices are intended to enhance the precision of the FC graphs G^T and G^B.

We provide Fig. 4 for visual clarification. Figure 4 illustrates the adjacency matrix of a graph G^B encompassing five frequency bands, each consisting of 19x19 channel matrix, as depicted on the left side. The dimension of this adjacent matrix is $E \in \mathbb{R}^{(5\times4)\times(5\times4)}$. In this matrix, each row represents the connections between an electrode channel and all other channels across different frequency bands. Since these channels belong to different frequency bands, their correlations should be adjusted according to the strength of coupling, as measured by a coupling rate κ. We categorize coupling degrees into three levels: strong coupling (self, θ-γ, α-γ, θ-α), medium coupling (β-γ, α-β, δ-θ), and weak coupling (δ-α, δ-β, δ-γ, β-θ). As the coupling degree decreases, the correlation naturally diminishes further, as measured by κ^2. Drawing from these discussions, we formulate the coupling matrix $\{\{c_{bd,ij}\}_{i,j=1}^{N}\}_{b,d}^{B}$. This matrix is employed to enhance the correlations between channels across bands, yielding $e_{bd,ij} = e_{bd,ij} \cdot c_{bd,ij}$. This approach guarantees that channels demonstrating higher degrees of cross-frequency coupling display stronger correlations compared to those with lower degrees of cross-frequency coupling, the complete coupling matrix onstruction is provided in algorithm 2.

Figure 4 illustrates the adjacency matrix of the graph G^T, assuming the graph contains three patches, each containing four channels, as shown on the left.In this matrix, each row presents a channel's connections with other channels across all patches. Since these channels are located in different patches, their correlations should decrease with increasing distance, as measured by a decay rate η. As the temporal gap expands, correlations naturally decline further, measured by η^2. Drawing from these discussions, we formulate the decay matrix $\{\{o_{tr,ij}\}_{i,j=1}^{N}\}_{t,r}^{L'}$. This matrix is employed to enhance the correlations between channels across bands, yielding $e_{tr,ij} = e_{tr,ij} \cdot o_{tr,ij}$. This approach guarantees that EEG channel channels located in close temporal proximity demonstrate stronger correlations compared to those situated further apart in time.

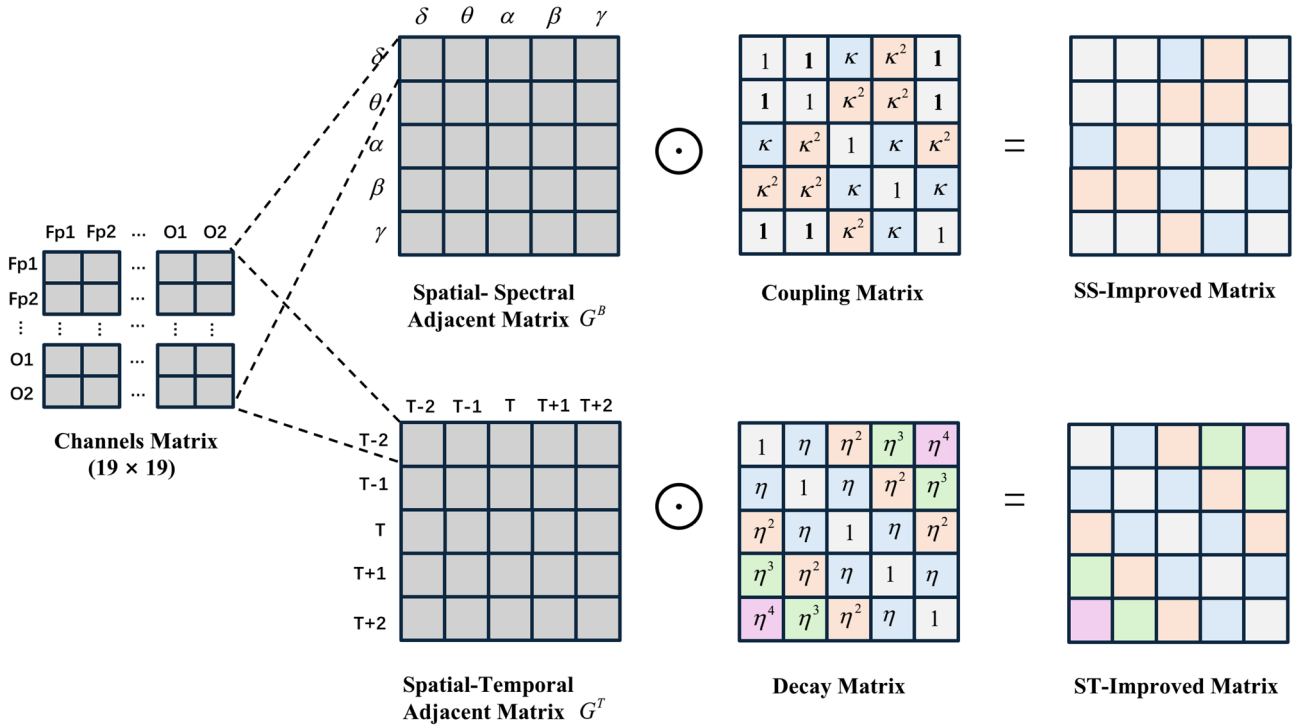


Fig. 4. In the schematic diagram illustrating the enhanced domain adjacency matrix based on correlation, each segment of the fully connected domain adjacency matrix corresponds to a 19×19 channel matrix. The coupling matrix (upper portion) quantifies the coupling strength (ranging from 0 to 1) between different frequency bands and performs a Hadamard Product with the adjacency matrix in the spatial-frequency graph to achieve enhancement. Conversely, the attenuation matrix (lower portion) quantifies the distance (ranging from 0 to 1) between distinct time intervals and carries out a Hadamard Product with the adjacency matrix in the spatio-temporal graph, thereby realizing enhancement.

Input: $\mathbf{E}^B \in \mathbb{R}^{(B\times N)\times(B\times N)}$: Initial cross-band FC adjacency matrix
$\mathbf{C} \in \mathbb{R}^{B\times B\times N\times N}$: Spectral coupling tensor (contains κ, κ^2 weights)
B: Number of frequency bands
N: Channels per band
Output: $\mathbf{E}^{B*}$: Refined adjacency matrix with spectral coupling

Step 1: Cross-band Coupling Enhancement
for $b \leftarrow 1$ **to** B **do**
  for $d \leftarrow 1$ **to** B **do**
    for $i \leftarrow 1$ **to** N **do**
      for $j \leftarrow 1$ **to** N **do**
        idx_row $\leftarrow (b-1)\times N + i$ // Row index for (band b, channel i)
        idx_col $\leftarrow (d-1)\times N + j$ // Column index for (band d, channel j)
        if $(b,d) \in \mathscr{S}_{strong}$ **then**
          $\mathbf{C}[b,d,i,j] \leftarrow \kappa_{\text{strong}}$
        else if $(b,d) \in \mathscr{S}_{medium}$ **then**
          $\mathbf{C}[b,d,i,j] \leftarrow \kappa_{\text{medium}}$
        else
          $\mathbf{C}[b,d,i,j] \leftarrow \kappa_{\text{weak}}$
        end
        $\mathbf{E}^B[\text{idx_row}, \text{idx_col}] \leftarrow \mathbf{E}^B[\text{idx_row}, \text{idx_col}] \cdot \mathbf{C}[b,d,i,j]$
      end
    end
  end
end

return $\mathbf{E}^{B*} \leftarrow \mathbf{E}^B$

Algorithm 2. Enhanced FC graph construction with spectral coupling.

Multi-scale graph convolution

Using the constructed fully connected (FC) graph, the next step is to capture the spatial-temporal and spatial-spectral dependencies in EEG data for representation learning. A straightforward approach involves applying graph convolution across the entire graph. However, when dealing with data that exhibit local structural characteristics, such as EEG, traditional graph convolutional networks (GCNs) may not effectively capture the local dependencies inherent in a fully connected graph. Multi-scale graph convolutions can effectively capture both local and global dependencies within a graph by simultaneously aggregating neighborhood information across varying ranges[41,42]. Thus, we propose a Multi-Scale Graph Convolution method, which employs multi-scale receptive fields to simultaneously capture fine-grained information from local neighborhoods (e.g., one neighbor) and coarse-grained information from global neighborhoods(e.g., k neighbors). Additionally, we introduce learnable fusion weights that enable the model to dynamically adjust the contributions of features at different scales based on the data, further enhancing its expressive capacity.

We partition the FC graph into k scales by applying a moving window of size $k+1$, with the window shifting by one unit at each step. For simplicity, we refer to the different bands in the spatial-spectral graph and the different timestamps in the spatial-temporal graph as patches. Fig. 3c provides a visual illustration of a fully connected graph (FC graph), assuming it contains five patches, each with 19 channels (specific channels are omitted for simplicity). In this example, a window of size two slides with a stride of one, generating four windows that constitute the first-scale FC graph. Similarly, a window of size three slides with a stride of one, resulting in three windows for the second-scale FC graph. A window of size four, moved with a stride of one, produces two windows for the third-scale FC graph. Subsequently, graph neural networks are applied within each window.

In particular, drawing on previous studies[43], we utilize Message Passing Neural Networks (MPNNs) as the fundamental component, which are a type of Graph Neural Networks, to effectively capture dependencies across different scales of the graph. Our proposed multi-scale Graph Convolution includes the propagation, update, and aggregation phases. During the propagation phase, the central node receives information transmitted from its neighboring nodes. Given the central node $x^k_{p,i}$ of the w-th window in the k-th scale, it possesses a set of neighboring nodes that span $k+1$ patches within the same window. The central node exhibits a correlation with its neighbors as $\{\{x^k_{q,j}\}_{j=1}^N\}_{q=w-\frac{k+1}{2}}^{w+\frac{k+1}{2}}$. The central node has correlations with its neighbors as $\{\{e^k_{pq,ij}\}_{j=1}^N\}_{q=w-\frac{k+1}{2}}^{w+\frac{k+1}{2}}$. Following the propagation phase, we obtain the propagated features

$z_{p,i}^k = \sum_{q=w-\frac{k+1}{2}}^{w+\frac{k+1}{2}} \sum_{j=1}^{N} x_{q,j}^k e_{pq,ij}^k$. In the update phase, we employ a nonlinear function to update the propagated channel features, specifically $h_{q,i}^k = f_g(z_{q,i}^k | w_g)$, where f_g as the nonlinear activation function, and w_g represents the weight matrix. In the aggregation phase, we initialize a trainable weight parameter α^k for each scale k and normalize these parameters using the softmax function to obtain weight coefficients α^k, satisfying $\sum_{k=1}^{K} \alpha^k = 1$. Subsequently, we multiply the features h^k from different scales by their corresponding weight coefficients α^k and perform a summation to obtain the fused features $F = \sum_{k=1}^{K} \alpha^k H^k$. Subsequently, the features from different scales are multiplied by their corresponding weight coefficients and then summed to produce the fused features.

Overall, the Multi-scale Graph Convolution facilitates information propagation and feature updating across multiple receptive fields. For each scale, the Graph Convolution propagates channel information across $k+1$ patches based on the correlations among all channels. This propagation enables the comprehensive capture of dependencies within each window, facilitating the update of channel features. During the update phase, a nonlinear function is introduced to refine the channel features, thereby enhancing the model's ability to learn effective representations. After updating the channel features by capturing spatial and temporal/spectral dependencies, learnable fusion weights are employed to dynamically adjust the contributions of features at each scale according to the data's characteristics. This strategy allows for a more effective capture of complex spatial-temporal and spatial-spectral dependencies, thereby improving the model's adaptability.

Bi-path attention fusion

The bi-path architecture can jointly optimize deep semantic abstraction and high-resolution spatial representations, achieving a dynamic balance between global context modeling and local details within a unified framework[44,45]. Therefore, we further optimize multi-domain correlated information through a dual-path structural network, extracting spatiotemporal and spatial-spectral domain features from multi-domain data via two distinct paths. In earlier approaches, feature fusion was predominantly performed using simple concatenation operations. Although this method is effective, it introduces several issues: (1) Concatenation-based feature fusion tends to incorporate irrelevant and redundant information, increasing model complexity; and (2) It fails to effectively identify and leverage the complex interactions between different features. To address these challenges, we have designed a dual-attention fusion module inspired by cross-modal attention computations[46]. The Bi-Path Attention Fusion, as shown in Fig. 3 , follows the standard dot-product attention[40].

In detail, given the extracted spatial-temporal feature $\mathbf{F}^T \in \mathbb{R}^{n_T \times d_T}$ and spatial-spectral feature $\mathbf{F}^B \in \mathbb{R}^{n_B \times d_B}$(where n_T, n_B denote sequence lengths, d_T, d_B feature dimensions), we first project both modalities into a shared latent space through learnable transformations:

$$\mathbf{Q}^S = \mathbf{F}^B \mathbf{W}_Q + \mathbf{b}_Q, \quad \mathbf{K}^S = \mathbf{F}^T \mathbf{W}_K + \mathbf{b}_K, \quad \mathbf{V}^S = \mathbf{F}^T \mathbf{W}_V + \mathbf{b}_V, \tag{4}$$

where $\mathbf{W}_Q \in \mathbb{R}^{d_B \times d}$(latent dimension d), $\mathbf{W}_K, \mathbf{W}_V \in \mathbb{R}^{d_T \times d}$ are projection matrices and $\mathbf{b}_Q, \mathbf{b}_K, \mathbf{b}_V \in \mathbb{R}^d$ are bias terms.

The cross-domain attention mechanism then computes similarity scores between the spatial-spectral queries and spatial-temporal keys:

$$\mathbf{A}^S = \text{softmax}\left(\frac{\mathbf{Q}^S (\mathbf{K}^S)^\top}{\sqrt{d}}\right) \in \mathbb{R}^{n_B \times n_T}, \tag{5}$$

where the scaling factor $1/\sqrt{d}$ prevents gradient vanishing issues. The resultant attention weights $\mathbf{A}^S$ determine how to adaptively aggregate spatial-temporal values $\mathbf{V}^S$:

$$\mathbf{F}^{TB} = \mathbf{A}^S \mathbf{V}^S \in \mathbb{R}^{n_B \times d}. \tag{6}$$

To preserve original spectral information and stabilize training, we employ residual connection with layer normalization (LayerNorm):

$$\mathbf{F}^{TB} = \text{LayerNorm}\left(\mathbf{F}^{TB} + \mathbf{F}^B \mathbf{W}_{\text{res}}\right), \tag{7}$$

where $\mathbf{W}_{\text{res}} \in \mathbb{R}^{d_B \times d}$ aligns dimensionalities for additive fusion.

The bi-attention fusion (BAF) establishes dual-aspect complementarity: the spatial-spectral features $\mathbf{F}^B$ serve as queries to dynamically identify relevant components in the spatial-temporal features $\mathbf{F}^T$ through cross-domain interaction, ultimately improving the detection of early-stage dementia manifestations.

Experimental results

Dataset

We conducted experiments on two datasets containing resting-state EEG signals from patients with Alzheimer's disease (AD) and other forms of dementia: the AHEPA dataset[47] and the CAUEEG dataset[48].

AHEPA Dataset includes resting-state, eyes-closed EEG recordings from 36 patients with AD, 23 patients with frontotemporal dementia (FTD), and 29 normal controls (NC). All participants were assessed for cognitive and neuropsychological status using the Mini-Mental State Examination (MMSE). EEG signals were recorded using 19 scalp electrodes (Fp1, Fp2, F7, F3, Fz, F4, F8, T3, C3, Cz, C4, T4, T5, P3, Pz, P4, T6, O1, O2) and two

reference electrodes, with electrode placement based on the international 10–20 system. Data acquisition was performed at a sampling rate of 500 Hz.

CAUEEG Dataset contains resting-state, eyes-closed EEG data from 1,187 participants, including 459 normal individuals, 417 patients with mild cognitive impairment (MCI), and 311 patients with dementia (DEM), including AD and other types of dementia. Each recording consists of 19 channels with electrode positions set according to the international 10–20 system (Fp1, F3, C3, P3, O1, Fp2, F4, C4, P4, O2, F7, T3, T5, F8, T4, T6, Fz, Cz, Pz). EEG signals were recorded at a sampling rate of 200 Hz while participants were in a comfortable, resting, eyes-closed state. For more detailed information on both datasets, please refer to previously published works[47,48].

The preprocessing pipeline of the EEG signals is as follows. First, a Butterworth band-pass filter 0.5–45 Hz was applied and the signals were re-referenced to A1–A2. Then, the Artifact Subspace Reconstruction routine (ASR) which is an EEG artifact correction method included in the EEGLab Matlab software was applied to the signals, removing bad data periods which exceeded the max acceptable 0.5 second window standard deviation of 17, which is considered a conservative window. Next, the Independent Component Analysis (ICA) method (RunICA algorithm) was performed, transforming the 19 EEG signals to 19 ICA components. ICA components that were classified as "eye artifacts" or "jaw artifacts" by the automatic classification routine "ICLabel" in the EEGLAB platform were automatically rejected.

For the AHEPA dataset, we divided the data into two subsets: AD-NC and FTD-NC. In each subset, we applied a leave-one-subject-out cross-validation strategy, ensuring that the training and testing sets were from different participants. For the CAUEEG dataset, we partitioned the data into 80%, 10%, and 10% for training, validation, and testing, respectively, ensuring that the training and testing sets came from different subjects, following previous work[48]. Given the complexity of medical diagnosis and data imbalance, the primary classification performance metrics used include accuracy, recall, and specificity. Accuracy measures overall classification correctness, recall focuses on missed diagnoses, and specificity addresses misdiagnosis rates. These metrics are derived from a confusion matrix. For the AHEPA dataset, for example, TP represents the number of samples correctly diagnosed as AD, TN represents the number of samples correctly diagnosed as non-AD, FP represents the number of samples incorrectly diagnosed as AD, and FN represents the number of samples incorrectly diagnosed as non-AD. The specific formulas for calculating these evaluation metrics are as follows:

$$Accuracy = \frac{TP + TN}{TP + TN + FP + FN} \tag{8}$$

$$Sensitivity = \frac{TP}{TP + FN} \tag{9}$$

$$Specificity = \frac{TP}{TP + FN} \tag{10}$$

Experimental setup

For the AHEPA dataset, we first performed preprocessing steps, including denoising and artifact removal, on the collected data and downsampled the sampling rate to 200 Hz. Next, we divided each trial into multiple samples using non-overlapping 5-s windows. For each 5-s sample, we further segmented the data into five 1-s sub-samples, with the raw data serving as input for the spatiotemporal path. Simultaneously, we applied the Fast Fourier Transform (FFT) to compute the power spectral density (PSD) features of each channel across five frequency bands, generating 5 sub-samples for the frequency-spatial path: including delta(δ) waves(0.5–4 Hz), theta (θ) waves (4–8 Hz), alpha (α) waves (8–13 Hz), beta (β) waves (13-25 Hz), and gamma (γ) waves (25–45 Hz). For the CAUEEG dataset, we applied similar preprocessing steps, retained the original sampling rate of 200 Hz, and conducted data segmentation and feature extraction following the same methods.

Our model was implemented using the PyTorch framework and trained on an NVIDIA 3060 Ti. In the experimental section, AdamW was used as the optimizer, with a linear warm-up strategy for learning rate adjustments. Table 1 presents the parameter settings used in our study, including configurations for the Bi-MCGNN, correlation matrix, multi-scale graph convolution, and Bi-path attention fusion.

Model	Parameters	Dataset	
		APEHA	CAUEEG
Bi-MCGNN	Epochs	100	100
	Learning rate	3E–05	1.9E–05
	BatchSize	32	512
	Dropout	0.4	0.2
	Sample size	1000	1000
Correlation matrix	Decay rates	0.9	0.9
	Coupling rate	0.7	0.7
Multi-scale graph convolution	Scale number	4	4
Bi-path attention fusion	Number of encoder layers	1	1
	Attention head	2	4

Table 1. Parameters settings.

	AD-NC			FTD-NC		
	Accuracy (%)	Sensitivity (%)	Specificity (%)	Accuracy (%)	Sensitivity (%)	Specificity (%)
MLP[49]	75.79±0.98	76.82±0.92	74.96±1.42	73.91±0.95	76.36±0.87	72.34±0.85
SVM[50]	83.31±0.67	84.99±0.64	81.96±0.69	80.61±0.75	82.46±0.95	79.44±0.86
ViTs[39]	84.45±1.87	86.78±1.46	81.87±1.45	82.34±0.74	84.32±0.85	80.76±0.91
EEG Conformer[51]	85.41±1.05	87.42±1.33	82.56±1.25	84.05±0.89	85.45±0.93	84.03±0.78
ACRNN[52]	86.08±0.68	86.92±0.87	85.39±0.57	85.64±0.47	88.5±0.49	83.82±0.57
CoBFormer[53]	87.12±0.89	88.53±0.95	86.03±0.84	86.31±0.67	87.42±0.76	85.64±0.85
GCN[54]	88.19±0.54	90.47±0.85	86.36±0.47	87.57±0.48	88.62±0.58	86.9±0.78
DGCNN[55]	89.12±0.67	91.67±0.68	87.08±0.48	87.83±0.76	89.42±0.58	86.81±0.57
BI-MCGNN	**91.25±0.38**	**93.32±0.46**	**89.58±0.42**	**89.37±0.25**	**91.82±0.31**	**87.81±0.34**

Table 2. The performance on the AHEPA dataset. Significant values are in bold.

		Sensitivity (%)			Specificity (%)		
	Accuary	NC	MCI	Dementia	NC	MCI	Dementia
MLP	59.29±0.92	79.95±1.53	44.98±2.45	47.96±1.32	67.78±1.55	86.8±1.29	83.22±1.45
SVM	69.92±0.89	88.94±1.03	51.97±1.23	65.94±1.53	74.8±1.04	91.81±0.98	87.38±1.05
ACRNN	71.8±0.88	94.95±0.68	55.95±0.96	58.89±0.87	74.37±0.87	92.15±1.04	89.99±0.79
ViTs	73.67±1.14	92.45±1.42	60.43±1.14	59.53±1.23	75.38±1.05	89.53±1.51	91.53±1.14
EEG conformer	74.75±1.08	91.92±1.21	69.9±0.96	55.92±1.12	78.37±1.21	90.93±1.58	91.74±1.07
CoBFormer	76.66±1.52	89.03±1.32	63.58±1.53	60.68±1.15	86.24±1.05	84.58±1.26	93.16±0.86
GCN	76.98±0.84	93.88±0.87	59.93±0.67	74.92±0.95	79.8±0.93	94.48±1.01	90.45±0.77
DGCNN	78.27±0.95	95.09±0.78	**71.97±0.81**	61.91±0.81	80.62±0.83	92.65±0.97	**93.12±0.79**
BI-MCGNN	**80.21±0.76**	**96.94±0.53**	64.92±0.54	**76.05±0.78**	**81.81±0.75**	**95.41±0.84**	92.34±0.68

Table 3. The performance on the CAUEEG dataset. Significant values are in bold.

Analysis and comparison of results

We compared our method with traditional approaches and advanced graph neural network (GNN) models, including MLP, SVM, ViTs, EEG Conforme, CoBFormer, ACRNN, GCN and DGCNN. To ensure a fair comparison, we adopted the same data processing and experimental setups across all models and performed five-fold cross-validation for robust statistical verification. The comparison results, presented in Tables 2 and 3, demonstrate the significant effectiveness of BI-MCGNN. Due to its ability for automatic feature extraction, most deep learning models outperformed traditional methods (MLP and SVM). ACRNN can simultaneously capture temporal and spatial domain information, achieving an accuracy of 86.08% on the AD-NC task of the AHEPA dataset. Similarly, EEG Conformer integrates CNNs with a Transformer architecture to simultaneously capture both local and global features. In addition, the performance of ViTs is suboptimal; we infer that the grid-based modeling assumption conflicts with the non-Euclidean topological structure of EEG signals (disrupting physiological correlations among brain regions), and that the required training data far exceeds the current scale of EEG datasets. Furthermore, although CoBFormer achieves relatively good results, it is not the best-performing model. We hypothesize that its limitations stem from the strong association between the pathological features of AD/MCI and changes in connectivity strength of specific brain regions. The global-local attention balance mechanism in CoBFormer may weaken the task-relevant critical topological dependencies, thereby impacting model performance. GCN extracts spatial features from signals based on a fixed graph, while DGCNN can adaptively learn the intrinsic relationships between different channels by optimizing the adjacency matrix. As a result, DGCNN's performance is approximately 0.93% better than that of GCN. BI-MCGNN achieved the highest performance on this task.

In further experiments, we conducted a comprehensive comparison of BI-MCGNN on EEG diagnostic tasks for FTD and dementia to fully assess its performance. The results of this comparative study are detailed in Tables 2 and 3. Analysis shows that BI-MCGNN consistently outperforms other models across different datasets, achieving higher accuracy by 91.25%, 89.37%, and 80.21% in the three tasks, respectively.

Additionally, we compared our model with other baseline models on the AHEPA and CAUEEG datasets separately to verify its superiority in EEG-based detection of neurocognitive disorders (see Table 4 for details). The results show that BI-MCGNN outperforms all other methods on both datasets, improving accuracy by 2.35% on the AD-NC task and 3.07% on the FTD-NC task in the AHEPA dataset. Similar improvements were observed in the CAUEEG dataset, where our method outperformed the next best method by 3.55% in terms of accuracy. These advancements highlight the importance of fully capturing the spatiotemporal and spatial-spectral dependencies in EEG data, leading to superior performance compared to other methods. Our proposed graph-based model effectively explores spatial-spectral-temporal domain information in EEG signals.

Reference	Features	Classifier	AHEPA			CAUEEG			Accuracy(%)
			NC	AD	FTD	NC	MCI	DEM	
Miltiadous[56]	Band power and coherence characteristics	CNN+transformer	✓	✓					84.97
			✓		✓				74.96
Chen[22]	Raw data and Spectralimage	CNN and ViT	✓	✓					88.19
			✓		✓				83.41
Parihar[57]	Time and frequency domain features	Random Forest	✓	✓					88.9
			✓		✓				84.1
Tzimourta[58]	Time and frequency domain features	Random forest	✓		✓				86.3
Kim[48]	Raw data and spectral image	Ensemble model				✓	✓	✓	76.66
BI-MCGNN	PSD and Raw data	GCN	✓	✓					**91.19**
			✓		✓				**89.59**
						✓	✓	✓	**80.21**

Table 4. Performance of popular features and classifiers implemented on the same dataset.

Furthermore, we are considering the use of fully connected graphs and multi-level graph convolutions to better capture dependencies under the DCDT and DCDB frameworks.

Ablation studies

To verify the effectiveness of the model, we conducted ablation experiments on two datasets. The ablation studies were divided into two types: (1) evaluating the effectiveness of FC graph construction, multi-scale graph convolution, bi-path attention fusion, and the correlation matrix, and (2) assessing the bi-path structure to validate the benefit of simultaneously utilizing spatial-spectral-temporal domain features.

In the first set of ablation studies, we evaluated the effectiveness of the proposed modules by designing four variants as follows: In the first variant, "w/o FC," we excluded FC graph construction and instead followed traditional methods[43,59], constructing and convolving the graph for each patch separately (e.g., different timestamps in the spatiotemporal domain or different bands in the spatial-spectral domain). The second variant, "w/o GC," integrated FC graph construction but omitted multi-scale graph convolution, thus failing to capture local spatiotemporal (ST) and spatial-spectral (SS) dependencies. The third variant, "w/o fusion," excluded the Bi-Path Attention Fusion module, which is designed to fuse multiple features. Lastly, the "w/o Correlation" variant omitted the correlation matrix used to enhance the constructed FC graph. These variants were compared against the full model.

Tables 5 and 6 present the results of the ablation studies on the two datasets. The performance analysis was conducted using the AD-NC task from the AHEPA dataset as an example. Compared to the "w/o FC" variant, the full model achieved a 2.04% improvement, demonstrating the importance of effective feature learning via the comprehensive modeling of spatiotemporal (ST) and spatial-spectral (SS) dependencies through the FC graph. When multi-scale graph convolution was excluded ("w/o GC"), the performance dropped by 2.33%, indicating that multi-scale convolution improves representation learning by capturing both local and global dependencies. Moreover, comparing the "w/o fusion" variant with the full model revealed that the Bi-Path Attention Fusion module enhances performance by explicitly capturing inter-feature relationships and filtering redundant information via adaptive feature weighting using self-attention mechanisms. Finally, excluding the correlation matrix led to a 1.05% performance decrease, underscoring the importance of using decay and correlation matrices to refine the constructed FC graph. These results were consistent across the FTD-NC task and the CAUEEG dataset. Overall, the findings highlight the critical role of modeling and fusing comprehensive ST and SS dependencies in EEG data to enable more effective representation learning.

We conducted a second ablation study to evaluate the effectiveness of integrating the two pathways. We developed two variants as follows: In the first variant, "w/o SS," we removed the Spatial-Spectral pathway to assess the impact of utilizing the Spatio-Temporal features of EEG signals. In the second variant, "w/o ST," we eliminated the Spatial-Temporal pathway to examine the effect of leveraging the spatial-spectral features of EEG signals. As presented in Tables 7 and 8, the performance of the "w/o ST" variant exceeds that of the "w/o SS" variant, indicating that extracting features in the spatial and spectral domains is more effective than in the spatial and temporal domains. Furthermore, BI-MCGNN outperforms both variants, demonstrating that our model effectively fuses spatial, spectral, and temporal features to enhance classification accuracy.

Feature importance analysis

To facilitate interpretability analysis, typical AD patients (MMSE=17, CDR=1) was selected from the dataset as the test case for computing feature, node, and edge importance in model predictions. The results are illustrated in Fig. 5. The feature importance plot (left panel) demonstrates that the theta frequency band exhibits the highest contribution to predictions, with a marked predominance over other bands, particularly beta and delta. The middle panel reveals that the model primarily focuses on brain regions associated with the temporal lobe (electrodes Fp1 and Fp2), parietal lobe (electrodes P3, Pz, and P4), and occipital lobe (electrodes O1 and O2), consistent with clinical studies of AD pathology. Finally, edge correlation analysis (right panel) identifies the strongest nodal relationships among posterior regions adjacent to electrode O2, aligning with the node importance findings. In particular, the standard deviation of these edge correlations (0.0127) is significantly

Model	AD-NC			FTD-NC		
	Accuary (%)	Sensitivity (%)	Specificity (%)	Accuary (%)	Sensitivity (%)	Specificity (%)
w/o FC	89.21	90.52	88.16	87.22	89.46	85.78
w/o GC	88.92	91.5	86.86	86.64	88.94	85.17
w/o fusion	89.7	91.91	87.92	87.39	89.95	85.76
w/o correlation	90.2	92.41	88.43	88.03	90.36	86.53
Complete	**91.25**	**93.32**	**89.58**	**89.37**	**91.82**	**87.81**

Table 5. Ablation studies on different components on the AHEPA dataset. Significant values are in bold.

Model	Accuary (%)	Class-wise accuracy (%)			Sensitivity (%)			Specificity (%)		
		NC	MCI	DEM	NC	MCI	DEM	NC	MCI	DEM
w/o FC	78.12	86.01	83.38	86.85	94.33	62.74	74.84	80.77	94.56	91.12
w/o GC	77.48	85.46	83.08	86.43	93.38	62.48	74.11	80.46	94.23	90.8
w/o fusion	78.37	86.23	83.64	86.86	94.83	63.52	73.97	80.81	94.53	91.44
w/o correlation	79.2	86.82	84.17	87.41	95.37	64.45	75.1	81.42	94.85	91.77
Complete	**80.21**	**87.66**	**84.69**	**88.07**	**96.94**	**64.92**	**76.05**	**81.81**	**95.41**	**92.34**

Table 6. Ablation studies on different components on the CAUEEG dataset. Significant values are in bold.

Model	AD-NC			FTD-NC				
	Accuary (%)	Sensitivity (%)	Specificity (%)	Accuary (%)	Sensitivity (%)	Specificity (%)		
w/o ST	88.07	90.52	86.09	87.71	89.13	86.81		
w/o SS	88.97	88.51	89.16	87.94	90.46	86.36		
ST+SS	**91.25**	**93.32**	**89.58**	**89.37**	**91.82**	**87.81**		

Table 7. Ablation studies on two-path structure on the AHEPA dataset. Significant values are in bold.

Model	Accuary (%)	Class-wise accuracy (%)			Sensitivity (%)			Specificity (%)		
		NC	MCI	DEM	NC	MCI	DEM	NC	MCI	DEM
w/o ST	76.96	85.02	82.51	86.4	92.4	60.8	75.86	80.36	94.27	90.15
w/o SS	77.88	85.72	83.27	86.77	93.34	62.74	75.39	80.92	94.39	90.82
ST+SS	**80.21**	**87.66**	**84.69**	**88.07**	**96.94**	**64.92**	**76.05**	**81.81**	**95.41**	**92.34**

Table 8. Ablation studies on two-path structure on the CAUEEG dataset. Significant values are in bold.

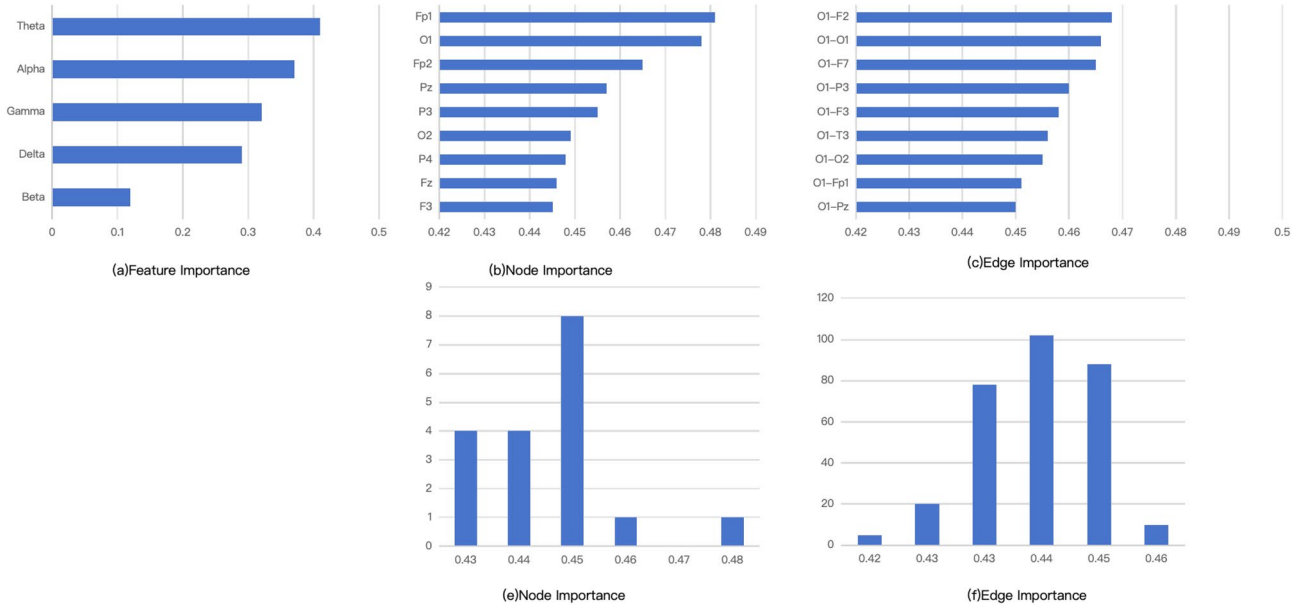


Fig. 5. Visualization of feature, node, and edge importance analysis for a typical AD patient (MMSE = 17, CDR = 1).

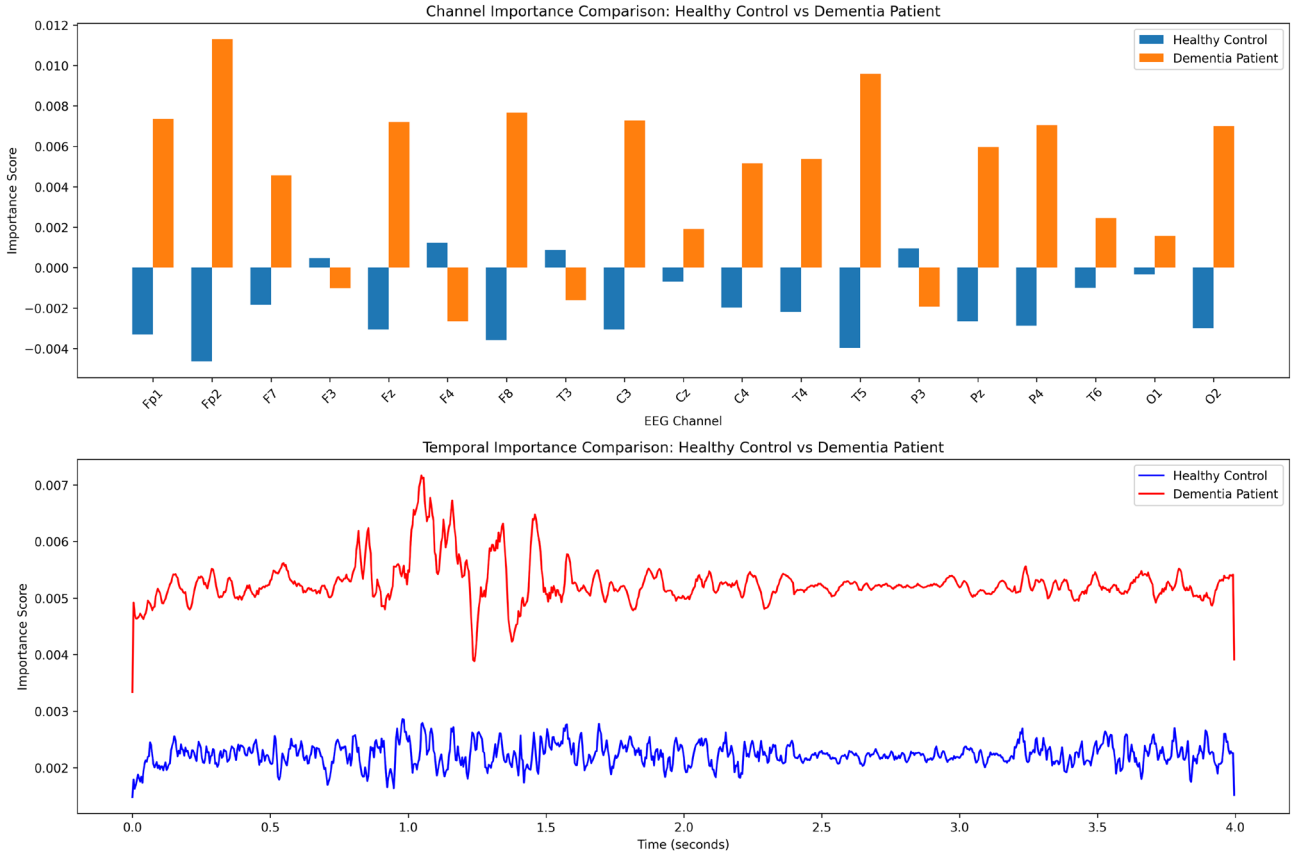


Fig. 6. Comparison of channel and temporal importance between healthy controls and dementia patients based on gradient-based interpretability.

higher than that of node importance metrics, providing more robust evidence for the interpretability of the proposed GNN model for predictions of this subject.

Gradient-based interpretability analysis

To gain deeper insight into the decision-making mechanism of the Bi-MCGNN model, we selected typical Alzheimer's Disease (AD) patients (MMSE = 17, CDR = 1) and normal controls from the dataset as test cases, and employed a gradient-based interpretability method (Grad-CAM) for model analysis. Figure 5 presents the comparison of importance distributions across EEG channels and temporal dimensions between healthy controls and dementia patients.

As shown in Fig. 6, there are significant regional differences in EEG channel importance between the healthy control group and dementia patients. The EEG signals of the healthy control group are primarily dominated by the prefrontal regions (Fp1, Fp2) and parietal regions (P3, Pz, P4), which play crucial roles in normal cognitive function. In contrast, the EEG signals of dementia patients are mainly dominated by the temporal regions (T3, T4, T5, T6), which is consistent with existing research indicating that dementia typically affects the temporal lobe regions[60]. This finding supports our hypothesis that dementia leads to changes in brain functional connectivity patterns, especially in the temporal lobe regions associated with memory and language processing.

Figure 6 specifically illustrates the temporal importance distribution patterns for both subject groups. While the temporal importance curve of healthy controls remains relatively stable with only minor fluctuations, indicating high temporal stability in healthy brain signal processing, the dementia group demonstrates significantly increased variability in their temporal importance patterns. These peaks of heightened importance correspond to abnormal waveforms or patterns in AD patients' EEG signals, suggesting impaired signal transmission caused by neuronal connectivity degradation.

These findings confirm that our bi-path multi-scale design can effectively integrate information from temporal, spatial, and frequency domains, providing a new perspective for early diagnosis of dementia.

Discussion

In order to facilitate the clinical translation of AI-driven neurodegenerative disease diagnostic technologies, it is essential to establish a substantive link between algorithmic performance and clinical needs. In this study, we propose a dual-pathway multi-scale graph neural network (Bi-MCGNN), which achieves promising classification accuracy across multiple datasets. The core contribution of this method lies in integrating the temporal, spatial, and spectral features via dual-pathway fusion, thereby addressing the current challenge of low

diagnostic precision in the detection of AD, FTD, and MCI. Compared to the traditional combination of the Mini-Mental State Examination (MMSE)[61] and cerebrospinal fluid analysis, our approach increases the three-class diagnostic sensitivity, including the MCI stage, from 68.3% to 80.21%. This advancement is significant for reducing the diagnostic cycle of dementia and further enhances the accuracy of distinguishing among individuals with MMSE scores near the critical range of 24- -26.

Despite the promising advancements, EEG-based dementia diagnosis still encounters several fundamental challenges. First, although both AD and FTD patients exhibit distinct spatial network topological differences, the spatial resolution of EEG signals is limited by skull attenuation, which may lead to missed detections of subtle frontal lobe lesions. Second, the heterogeneity in the progression from MCI to AD is reflected in EEG features: some patients demonstrate elevated power in the theta frequency band, whereas another subgroup presents decreased coherence in the alpha band. This biological heterogeneity necessitates the use of multiple follow-up data points for diagnostic revision in 7.3% of the cases. Furthermore, although synthetic functional connectivity graphs have been created through domain-specific correlation enhancement techniques, the small sample size (n = 214) may still constrain the model's ability to generalize to rare FTD subtypes[62] (e.g., the non-fluent variant of primary progressive aphasia). Future work will need to validate these findings in multi-ethnic cohorts.

In terms of clinical translation, this study aims to establish a collaborative diagnostic system in subsequent work. First, data security is ensured through k = 5 anonymization[63] and ϵ=0.87 differential privacy. Second, a review mechanism by neurologists is introduced: model predictions must be cross-verified against structural MRI or neuropsychological evaluations. These measures align with the World Health Organization (WHO) guidelines[64] on AI-mediated diagnostics. Nonetheless, we acknowledge current barriers to implementation in resource-limited environments. Consequently, future efforts will focus on cross-population validation and the optimization of real-time EEG processing for clinical diagnosis.

In future studies, we plan to address EEG heterogeneity by designing GNN architectures with online adjustment capabilities, employing dynamic weight allocation mechanisms to handle the divergent characteristics of theta and alpha subgroups. Subsequently, we intend to advance multimodal joint diagnostic endeavors, integrating EEG time-frequency features with diffusion tensor imaging (DTI) white matter integrity indices (fractional anisotropy) and plasma p-tau217 levels[65], among other biomarkers, to construct a multidimensional decision-fusion model.

Conclusion

To model the spatial-spectral-temporal dependencies in EEG data, we propose a novel bi-path multi-scale graph neural network that utilizes fully connected graphs for dementia diagnosis. Specifically, the proposed network is structured around a bi-path framework, capable of integrating spatiotemporal-spectral domain features into a unified model. It also adaptively assigns feature weights through an attention mechanism to capture complex relationships between features. For graph construction, we consider the correlation between DCDT and DCDB to connect electrode channels across all timestamps and frequency bands, thereby modeling both ST and SS dependencies in EEG data. Additionally, we propose decay and coupling matrices to enhance the fully connected graph by incorporating internal correlations within the domains, enabling a more comprehensive representation of dependencies. Next, we propose a multi-scale graph convolution that simultaneously captures both local and global information through multi-scale receptive fields. This convolution also introduces learnable fusion weights, enabling the model to dynamically adjust the contribution of features at different scales, thereby enhancing its expressive power. Our method is evaluated through extensive experiments, demonstrating its effectiveness in improving detection performance for AD and related dementias.

Data availability

This study analyzed publicly available datasets and uploaded code. This data can be found at: 1. The AHEPA Dataset is available via a publicly available link: https://openneuro.org/datasets/ds004504/versions/1.0.2. 2. The CAUEEG dataset used in this study was obtained from the official repository at https://github.com/ipis-mjkim/caueeg-dataset. To access this dataset, researchers are required to fill out a specific form as approval from the local ethics committee is necessary. After the response is reviewed, the dataset providers will send a mail containing a download link and password. 3. The code is available at https://gitcode.com/Kooooooooooo/Bi-Mcgnn2025.

Received: 18 November 2024; Accepted: 9 June 2025
Published online: 02 July 2025

References

1. Farina, F. R. et al. A comparison of resting state EEG and structural MRI for classifying Alzheimer's disease and mild cognitive impairment. *Neuroimage* **215**, 116795 (2020).
2. Ebrahimighahnavieh, M. A., Luo, S. & Chiong, R. Deep learning to detect Alzheimer's disease from neuroimaging: A systematic literature review. *Comput. Methods Prog. Biomed.* **187**, 105242 (2020).
3. Cohen, M. X. Where does EEG come from and what does it mean?. *Trends Neurosci.* **40**, 208–218 (2017).
4. Cao, J. et al. Brain functional and effective connectivity based on electroencephalography recordings: A review. *Hum. Brain Mapp.* **43**, 860–879 (2022).
5. Goldenberg, D. & Galván, A. The use of functional and effective connectivity techniques to understand the developing brain. *Dev. Cognit. Neurosci.* **12**, 155–164 (2015).
6. Zhang, K., Ye, Z., Ai, Q., Xie, X. & Liu, Y. Gnn4eeg: A benchmark and toolkit for electroencephalography classification with graph neural network. In *Companion of the 2024 on ACM International Joint Conference on Pervasive and Ubiquitous Computing*. 612–617 (2024).
7. Dauwels, J., Vialatte, F., Musha, T. & Cichocki, A. A comparative study of synchrony measures for the early diagnosis of Alzheimer's disease based on EEG. *NeuroImage* **49**, 668–693 (2010).

8. Vyšata, O., Vališ, M., Procházka, A., Rusina, R. & Pazdera, L. Linear and nonlinear EEG synchronization in Alzheimer's disease. *Neurophysiology* **47**, 46–52 (2015).
9. Supekar, K., Menon, V., Rubin, D., Musen, M. & Greicius, M. D. Network analysis of intrinsic functional brain connectivity in Alzheimer's disease. *PLoS Comput. Biol.* **4**, e1000100 (2008).
10. Klepl, D. et al. Characterising Alzheimer's disease with EEG-based energy landscape analysis. *IEEE J. Biomed. Health Inform.* **26**, 992–1000 (2021).
11. Jia, Z. et al. Graphsleepnet: Adaptive spatial-temporal graph convolutional networks for sleep stage classification. *In Ijcai* **2021**, 1324–1330 (2020).
12. Song, T., Zheng, W., Song, P. & Cui, Z. EEG emotion recognition using dynamical graph convolutional neural networks. *IEEE Trans. Affect. Comput.* **11**, 532–541 (2018).
13. Zhong, P., Wang, D. & Miao, C. EEG-based emotion recognition using regularized graph neural networks. *IEEE Trans. Affect. Comput.* **13**, 1290–1301 (2020).
14. Xing, T. et al. An adaptive multi-graph neural network with multimodal feature fusion learning for MDD detection. *Sci. Rep.* **14**, 28400 (2024).
15. Asadzadeh, S., Yousefi Rezaii, T., Beheshti, S. & Meshgini, S. Accurate emotion recognition using Bayesian model based EEG sources as dynamic graph convolutional neural network nodes. *Sci. Rep.* **12**, 10282 (2022).
16. Shan, X. et al. Spatial-temporal graph convolutional network for Alzheimer classification based on brain functional connectivity imaging of electroencephalogram. *Hum. Brain Mapp.* **43**, 5194–5209 (2022).
17. Radwan, M., Lind, P. G. & Yazidi, A. An interpretable graph based model for classification of EEG using directional functional connectivity. In *2024 IEEE International Symposium on Biomedical Imaging (ISBI)*. 1–5 (IEEE, 2024).
18. Cao, J., Yang, L., Sarrigiannis, P. G., Blackburn, D. & Zhao, Y. Dementia classification using a graph neural network on imaging of effective brain connectivity. *Comput. Biol. Med.* **168**, 107701 (2024).
19. Klepl, D., He, F., Wu, M., Blackburn, D. J. & Sarrigiannis, P. EEG-based graph neural network classification of Alzheimer's disease: An empirical evaluation of functional connectivity methods. *IEEE Trans. Neural Syst. Rehabil. Eng.* **30**, 2651–2660 (2022).
20. Wu, S. et al. Changes of brain functional network in Alzheimer's disease and frontotemporal dementia: A graph-theoretic analysis. *BMC Neurosci.* **25**, 30 (2024).
21. Klepl, D., He, F., Wu, M., Blackburn, D. J. & Sarrigiannis, P. Adaptive gated graph convolutional network for explainable diagnosis of Alzheimer's disease using EEG data. *IEEE Trans. Neural Syst. Rehabil. Eng.* **31**, 3978–3987 (2023).
22. Chen, Y., Wang, H., Zhang, D., Zhang, L. & Tao, L. Multi-feature fusion learning for Alzheimer's disease prediction using EEG signals in resting state. *Front. Neurosci.* **17**, 1272834 (2023).
23. Sanati Fahandari, A., Moshiryan, S. & Goshvarpour, A. Diagnosis of cognitive and mental disorders: A new approach based on spectral-spatiotemporal analysis and local graph structures of electroencephalogram signals. *Brain Sci.* **15**, 68 (2025).
24. Ieracitano, C. et al. A time-frequency based machine learning system for brain states classification via EEG signal processing. In *2019 International Joint Conference on Neural Networks (IJCNN)*. 1–8 (IEEE, 2019).
25. Pirrone, D., Weitschek, E., Di Paolo, P., De Salvo, S. & De Cola, M. C. EEG signal processing and supervised machine learning to early diagnose Alzheimer's disease. *Appl. Sci.* **12**, 5413 (2022).
26. Tavares, G., San-Martin, R., Ianof, J. N., Anghinah, R. & Fraga, F. J. Improvement in the automatic classification of Alzheimer's disease using EEG after feature selection. In *2019 IEEE International Conference on Systems, Man and Cybernetics (SMC)*. 1264–1269 (IEEE, 2019).
27. Fiscon, G., Weitschek, E., De Cola, M. C., Felici, G. & Bertolazzi, P. An integrated approach based on EEG signals processing combined with supervised methods to classify Alzheimer's disease patients. In *2018 IEEE International Conference on Bioinformatics and Biomedicine (BIBM)*. 2750–2752 (IEEE, 2018).
28. Mostile, G. et al. Differentiating neurodegenerative diseases based on EEG complexity. *Sci. Rep.* **14**, 24365 (2024).
29. Youssef, N. et al. Functional brain networks in mild cognitive impairment based on resting electroencephalography signals. *Front. Comput. Neurosci.* **15**, 698386 (2021).
30. Ieracitano, C., Mammone, N., Bramanti, A., Hussain, A. & Morabito, F. C. A convolutional neural network approach for classification of dementia stages based on 2d-spectral representation of eeg recordings. *Neurocomputing* **323**, 96–107 (2019).
31. Rad, E. M., Azarnoosh, M., Ghoshuni, M. & Khalilzadeh, M. M. Diagnosis of mild Alzheimer's disease by EEG and ERP signals using linear and nonlinear classifiers. *Biomed. Signal Process. Control* **70**, 103049 (2021).
32. Sheikhpour, R., Berahmand, K., Mohammadi, M. & Khosravi, H. Sparse feature selection using hypergraph Laplacian-based semi-supervised discriminant analysis. *Pattern Recognit.* **157**, 110882 (2025).
33. Sharifi, S. Enhancing kidney transplantation through multi-agent kidney exchange programs: A comprehensive review and optimization models. *arXiv preprint* arXiv:2502.07819 (2025).
34. Berahmand, K., Daneshfar, F., Salehi, E. S., Li, Y. & Xu, Y. Autoencoders and their applications in machine learning: A survey. *Artif. Intell. Rev.* **57**, 28 (2024).
35. Jiang, W.-B., Zhao, L.-M. & Lu, B.-L. Large brain model for learning generic representations with tremendous EEG data in BCI. *arXiv preprint* arXiv:2405.18765 (2024).
36. Jiang, W.-B., Zhao, L.-M. & Lu, B.-L. Large brain model for learning generic representations with tremendous EEG data in BCI. *arXiv preprint* arXiv:2405.18765 (2024).
37. Vicchietti, M. L., Ramos, F. M., Betting, L. E. & Campanharo, A. S. Computational methods of EEG signals analysis for Alzheimer's disease classification. *Sci. Rep.* **13**, 8184 (2023).
38. Khosravi, M., Parsaei, H., Rezaee, K. & Helfroush, M. S. Fusing convolutional learning and attention-based bi-LSTM networks for early Alzheimer's diagnosis from EEG signals towards IOMT. *Sci. Rep.* **14**, 26002 (2024).
39. Dosovitskiy, A. et al. An image is worth 16x16 words: Transformers for image recognition at scale. *arXiv preprint* arXiv:2010.11929 (2020).
40. Vaswani, A. Attention is all you need. *Advances in Neural Information Processing Systems* (2017).
41. Zhao, X. et al. Multiscale deep graph convolutional networks for intelligent fault diagnosis of rotor-bearing system under fluctuating working conditions. *IEEE Trans. Indus. Inform.* **19**, 166–176 (2022).
42. Liao, R., Zhao, Z., Urtasun, R. & Zemel, R. S. Lanczosnet: Multi-scale deep graph convolutional networks. *arXiv preprint* arXiv:1901.01484 (2019).
43. Wang, Y., Wu, M., Li, X., Xie, L. & Chen, Z. Multivariate time-series representation learning via hierarchical correlation pooling boosted graph neural network. *IEEE Trans. Artif. Intell.* **5**, 321–333 (2023).
44. Hu, J., Chen, S., Pan, Z., Zeng, S. & Yang, W. Perspective+ unet: Enhancing segmentation with bi-path fusion and efficient non-local attention for superior receptive fields. In *International Conference on Medical Image Computing and Computer-Assisted Intervention*. 499–509 (Springer, 2024).
45. Chen, Z., Yang, J., Feng, Z., Chen, L. & Li, L. Bishufflenext: A lightweight bi-path network for remote sensing scene classification. *Measurement* **209**, 112537 (2023).
46. Tsai, Y.-H. H. et al. Multimodal transformer for unaligned multimodal language sequences. In *Proceedings of the Conference. Association for Computational Linguistics. Meeting*. Vol. 2019. 6558 (NIH Public Access, 2019).
47. Miltiadous, A. et al. A dataset of scalp EEG recordings of Alzheimer's disease, frontotemporal dementia and healthy subjects from routine EEG. *Data* **8**, 95 (2023).

48. Kim, M.-J., Youn, Y. C. & Paik, J. Deep learning-based EEG analysis to classify normal, mild cognitive impairment, and dementia: Algorithms and dataset. *NeuroImage* **272**, 120054 (2023).
49. Rumelhart, D. E., Hinton, G. E. & Williams, R. J. Learning representations by back-propagating errors. *Nature* **323**, 533–536 (1986).
50. Boser, B. E. Proceedings of the 5th Annual ACM Workshop on Computational Learning Theory. Vol. 144 (1992).
51. Song, Y., Zheng, Q., Liu, B. & Gao, X. EEG conformer: Convolutional transformer for EEG decoding and visualization. *IEEE Trans. Neural Syst. Rehabil. Eng.* **31**, 710–719 (2022).
52. Tao, W. et al. EEG-based emotion recognition via channel-wise attention and self attention. *IEEE Trans. Affect. Comput.* **14**, 382–393 (2020).
53. Xing, Y., Wang, X., Li, Y., Huang, H. & Shi, C. Less is more: On the over-globalizing problem in graph transformers. *arXiv preprint* arXiv:2405.01102 (2024).
54. Kipf, T. N. & Welling, M. Semi-supervised classification with graph convolutional networks. *arXiv preprint* arXiv:1609.02907 (2016).
55. Song, T., Zheng, W., Song, P. & Cui, Z. EEG emotion recognition using dynamical graph convolutional neural networks. *IEEE Trans. Affect. Comput.* **11**, 532–541 (2018).
56. Miltiadous, A., Gionanidis, E., Tzimourta, K. D., Giannakeas, N. & Tzallas, A. T. Dice-net: a novel convolution-transformer architecture for Alzheimer detection in EEG signals. *IEEE Access* (2023).
57. Parihar, A. et al. Analysis of EEG signals with the use of wavelet transform for accurate classification of Alzheimer disease, frontotemporal dementia and healthy subjects using machine learning models. *Full Length Article* **14**, 43–3 (2024).
58. Miltiadous, A. et al. Alzheimer's disease and frontotemporal dementia: A robust classification method of EEG signals and a comparison of validation methods. *Diagnostics* **11**, 1437 (2021).
59. Jia, Z. et al. Graphsleepnet: Adaptive spatial-temporal graph convolutional networks for sleep stage classification. *In Ijcai* **2021**, 1324–1330 (2020).
60. Du, A. et al. Magnetic resonance imaging of the entorhinal cortex and hippocampus in mild cognitive impairment and Alzheimer's disease. *J. Neurol. Neurosurg. Psychiatry* **71**, 441–447 (2001).
61. Jack, C. R. Jr. et al. Nia-aa research framework: Toward a biological definition of Alzheimer's disease. *Alzheimer's Dementia* **14**, 535–562 (2018).
62. Jeong, J. EEG dynamics in patients with Alzheimer's disease. *Clin. Neurophysiol.* **115**, 1490–1505 (2004).
63. El Emam, K., Jonker, E., Arbuckle, L. & Malin, B. A systematic review of re-identification attacks on health data. *PloS one* **6**, e28071 (2011).
64. W. H. Organization et al. Ethics and governance of artificial intelligence for health: Who guidance: Executive summary. In *Ethics and Governance of Artificial Intelligence for Health: WHO Guidance: Executive Summary* (2021).
65. Palmqvist, S. et al. Discriminative accuracy of plasma phospho-tau217 for Alzheimer disease vs other neurodegenerative disorders. *Jama* **324**, 772–781 (2020).

Acknowledgements
This research was supported by Zhejiang Provincial Natural Science Foundation of China under Grant No.LGF21F020024, Youth Academic Team Project of Zhejiang Shuren University.

Author contributions
C.Z. collated the data, developed the software, drafted the manuscript, and analyzed and validated it. D.Z. led the conceptualization, methodology, reviewed, and edited the manuscript. D.Z. managed the funding and project oversight, and approved the final manuscript. All authors reviewed the manuscript.

Declarations

Competing interests
The authors declare no competing interests.

Additional information
Supplementary Information The online version contains supplementary material available at https://doi.org/10.1038/s41598-025-06519-3.

Correspondence and requests for materials should be addressed to C.Z.

Reprints and permissions information is available at www.nature.com/reprints.

Publisher's note Springer Nature remains neutral with regard to jurisdictional claims in published maps and institutional affiliations.

Open Access This article is licensed under a Creative Commons Attribution-NonCommercial-NoDerivatives 4.0 International License, which permits any non-commercial use, sharing, distribution and reproduction in any medium or format, as long as you give appropriate credit to the original author(s) and the source, provide a link to the Creative Commons licence, and indicate if you modified the licensed material. You do not have permission under this licence to share adapted material derived from this article or parts of it. The images or other third party material in this article are included in the article's Creative Commons licence, unless indicated otherwise in a credit line to the material. If material is not included in the article's Creative Commons licence and your intended use is not permitted by statutory regulation or exceeds the permitted use, you will need to obtain permission directly from the copyright holder. To view a copy of this licence, visit http://creativecommons.org/licenses/by-nc-nd/4.0/.

© The Author(s) 2025